

S264: Radio Astronomical Observing Course

Lab Report

Team A5

Aarathi Parameswaran

Purbita Kole

31st August 2023

Bonn-Cologne Graduate School of Physics and Astronomy

University of Bonn

Advanced Lab Course

Winter Semester 2023/2024

Contents

1	Introduction	1
2	Source Selection	2
2.1	Galaxy Candidate	2
2.2	Pulsar Candidate	3
3	Exploration of Telescope Design	4
3.1	Stockert 25m Radio Telescope	4
3.2	Construction of telescopes	4
3.2.1	Surface Accuracy	5
3.2.2	Aperture Blocking	7
3.3	Radiometer	8
3.3.1	Radiometer Equation	9
3.3.2	Spectrometer	10
3.3.3	Noise	10
4	Calibration using standard Milky Way source	11
4.1	Theoretical Background	11
4.1.1	Rayleigh-Jeans Approximation	11
4.1.2	Brightness Temperature and Antenna Temperature	11
4.2	Calibration Source Observation and Analysis	13
4.2.1	Observation	13
4.2.2	Determining Calibration factor and system temperature	15
5	Observing a nearby Galaxy	17
5.1	Observing Galaxy candidate	17
5.2	Calibrating galaxy spectrum	18
5.3	Calculating different masses of galaxy	21
6	Determining the distance of a pulsar	23
6.1	Chosen Pulsar and Integration Time	23
6.2	Data Reduction Process	23

7	Conclusion	28
8	Appendix	29
8.1	Source Galaxy Data	29
8.2	Galaxy observed	30
8.3	Gaussian Fits for Pulsar	31

1 Introduction

The aim of this lab is to gain experience and familiarize methods and techniques used in radio astronomy, with practical work to study the technical design of a single-dish radio telescope and data acquisition and reduction processes. The telescope introduced is the Stockert 25-m telescope located at Iversheim, as most high-frequency radio telescopes in the current day are built and operated the same way.

The experiment involves preparation by selecting suitable radio sources based on parameters of the given day of observation from online catalogues. On-site, the telescope's parts are identified and the telescope is set up to perform calibration with a standard Milky Way source and is used for data analysis in the subsequent steps. A nearby galaxy is observed and its parameters evaluated, and then a pulsar is observed to calculate its dispersion measure and thus, its distance [1].

2 Source Selection

In this lab course, we aim to do observations of various astrophysical objects in the radio frequency regime. In any astronomical observation, the visibility of the target is a preliminary effect to consider. As we are using observations in the radio regime, the airmass of Earth's atmosphere is not a preliminary factor, as radio frequencies especially around 1420 MHz are mostly transparent to Earth's atmosphere. The Stockert telescope is located in the Northern Hemisphere at the co-ordinates $50^{\circ} 34.2' N$ $6^{\circ} 43.4' E$ and at an altitude of 435 m. To obtain the location of the objects, we switch to the coordinates of the celestial sphere of the earth i.e. Right Ascension (RA) and Declination (Dec). In this observation we try to make all observations above 20° Dec, to avoid interference/obstructions from the earth's surface. The visibility of the objects on the date and time of observation is checked through the website [airmass](#).

2.1 Galaxy Candidate

For analysis, we need to calibrate our spectral data, with some previous measurements of the same astrophysical objects. We choose from the sources mentioned in a paper by Kalberla, Mebold and Reif [2]. Out of the three sources mentioned in the reference we choose **S7** as the candidate galaxy for source selection, as it is well above our declination limit.

In the radio astronomical observation of a galaxy, we want to measure the **HI** line of the galaxy. So the parameters taken into consideration are [1]:

- The **extent of the galaxy** should be well under the radio telescope's main beam width (0.5°), to capture the whole radio spectrum from that galaxy.
- **distance or radial velocity**: The galaxy should be in a local group of galaxies so that the telescope can capture a substantial amount of radio flux from that galaxy i.e. between -500 to 500 km s^{-1} . But its radial velocity should not be too close to the rotational velocity of the Milky Way galaxy, or the spectrum features might get smeared out.
- **High SNR**: We want to determine the brightness temperature of the galaxy, so even

though the spectrum should consist of the broad double horn spectrum, $HI - 21cm$ line width should be constrained to 100 km s^{-1} or so. For good SNR we also want a bright galaxy candidate so the galaxy preferably should have a mag below 15 in that radio frequency.

Galaxy	RA	Dec	Radial Vel (km/s)	Extend (arcmin)	HI 21 Mag	HI 21 50pc width (km/s)
NGC4736	192.7229	41.1194	308	15.14	13.36	207
NGC4395	186.4575	33.5461	313	13.18	11.53	98
NGC4258	184.7396	47.3039	447	18.62	11.2	421
NGC4244	184.3746	37.8075	247	19.5	11.02	170

Table 1: These constraints were applied in the [HEASARC](#) browser for the NEARGALCAT - Updated Nearby Galaxy Catalog [3]. The galaxy candidates in this table were obtained from that constrained data.

2.2 Pulsar Candidate

We observe radio pulses from the pulsar and want to analyse the dispersion measure (DM). So we need to consider the flux coming from pulsars. We need to find the proper distance for which radio flux is high and also the dispersion measure [1].

Name	RA	Dec	DM(pc/cm ³)	S1400(mJy)	Dist(kpc)
B0329+54	03:32:59	34:54:43	26.7641	203	1.695
B0355+54	03:58:54	54:13:14	57.142	23	1
B2021+51	20:22:50	51:54:50	22.54968	27	1.8

Table 2: The pulsar candidates are obtained from constraining DM from ANTF Pulsar Catalogue [4]

3 Exploration of Telescope Design

3.1 Stockert 25m Radio Telescope

The Stockert 25m radio telescope (Figure(1)) is located at the coordinates 50.56943°N 6.72179°E at Iversheim near Bad Münstereifel and consists of a 25m parabolic dish. It has an Elevation-Over-Azimuth construction and is fully steerable in the azimuthal direction and covers -2°to 90°in elevation. The dish is an aluminium mesh construction with a steel structure underneath [5, 6].



Figure 1: Stockert 25m Radio Telescope [5].

3.2 Construction of telescopes

Radio telescopes are constructed to collect electromagnetic radiation [1] and the construction aims to optimize this collection. One parameter is the dish size D : the larger the dish size, the more number of photons collected. An important quantity regarding the quality of the telescope is the Half-Power-Beam Width (HPBW). It limits the ability to separate two unresolved sources. The two sources cannot be resolved if they are closer than the HPBW. The HPBW is given by the equation:

$$HPBW[^\circ] = 58.9 \frac{\lambda[m]}{D[m]} \quad (1)$$

The two main types of construction for radio telescopes are Cassegrain and Gregory telescopes.

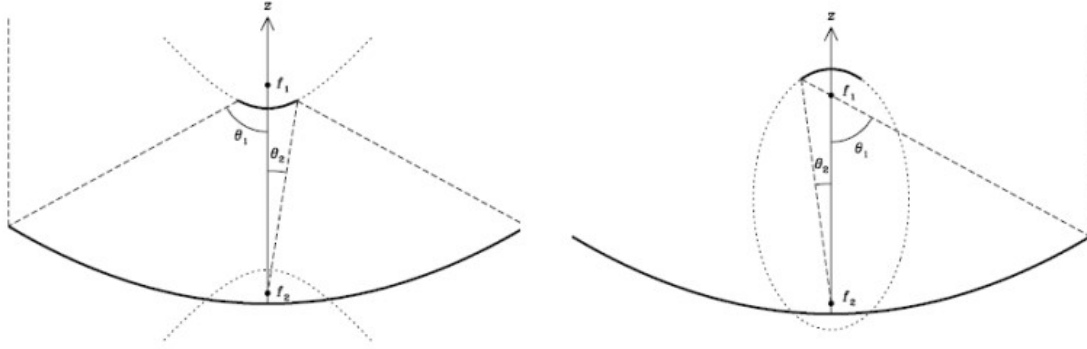


Figure 2: Optical designs of **Left:** Cassegrain telescope **Right:** Gregory telescope [1].

Cassegrain and Gregory constructions are affected by aperture blocking because both involve a secondary mirror (explained further in section 3.2.2).

The Gregory construction has the advantage of an additional focus over the Cassegrain, the prime focus of the primary mirror. So receivers can be installed at the two foci, primary and secondary. But in Cassegrain, due to the shape, only the secondary focus is accessible. The focal length of the primary mirror in Gregory construction is much shorter than that of Cassegrain, which makes the field of view of the primary focus much larger. Thus, because of the large f_1/D ratio the fast optics i.e. all the collected photons are concentrated in a compact focal plane, which allows high-speed recording of large portions of the sky using multi-beam receivers [1].

The 25m dish at Stockert used to be a Cassegrain telescope with a sub-reflector but the reflector has been removed and a feed is placed at the main focus, making it a prime focus telescope [5, 6].

3.2.1 Surface Accuracy

The surfaces of different radio telescopes are different based on the wavelengths that are to be observed by them, which determines the quality of the surface. The surface accuracy η is the parameter that quantifies the resolution and image quality of the telescope. The larger the surface accuracy of the primary mirror, the higher the resolution of the telescope.

The aim is to shape the primary mirror as an ideal parabola, and deviations from this shape (possibly caused by systematic deformations of the construction of the telescope) lead to a spatial shift of the focus. The roughness of the surface also degrades the imaging capabilities. As mentioned at the beginning of this section, the wavelength or the region of the electromagnetic spectrum that is to be observed plays a role in determining the design of the primary surface. For sub-mm telescopes, a surface quality comparable to optical telescopes is needed (a solid dish) while for dm telescopes the dish consists of wires or a mesh.

Due to the coherence of incoming radio waves, if the roughness of the surface corresponds to distortions of the order of $\frac{\lambda}{2}$ or $\frac{\lambda}{4}$, destructive interference will occur and a part of the signal will be lost. These deviations σ need to be minimized with respect to the corresponding wavelength λ . We approximate these deviations as a random distribution, the Gaussian distribution, around the ideal shape. The surface accuracy or smoothness parameter can be described qualitatively as:

$$\eta = \exp\left(-\left(\frac{4\pi\sigma}{\lambda}\right)^2\right) \quad (2)$$

The surface accuracy plotted against the ratio of the random surface variations and the wavelength can be seen in Figure(3).

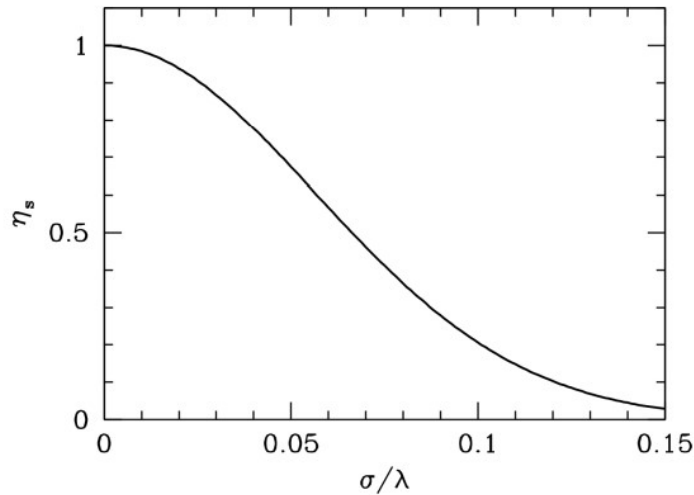


Figure 3: The smoothness of the surface as a function of the ratio of the surface random variation σ and the wavelength λ [1].

Thus we can see that the larger the wavelength λ , the larger the deviations σ are allowed

that keep surface accuracy constant. This also shows that mesh structures like the one in Stockert can be used to observe wavelengths of the decimeter order without significant losses [1].

3.2.2 Aperture Blocking

For most constructions of telescopes, including the ones mentioned above, the aperture of the telescope is blocked due to the secondary dish, which causes a reduction of the effective area of the main dish. This blocking causes losses by acting as an obstacle that lowers the number of incident photons, causing lower sensitivity and degraded angular resolution. There are also diffraction effects at the edges of these components that affect the image further. These effects can be seen in Figure(4). The figure shows a comparison of cases of the power distributions of an idealised unblocked aperture which results in the Airy disk pattern characteristic of a refracting telescope and that of the blocked aperture. With the blocked aperture, there are interference patterns caused by the secondary dish and the cross-like structure from the physical supporting legs.

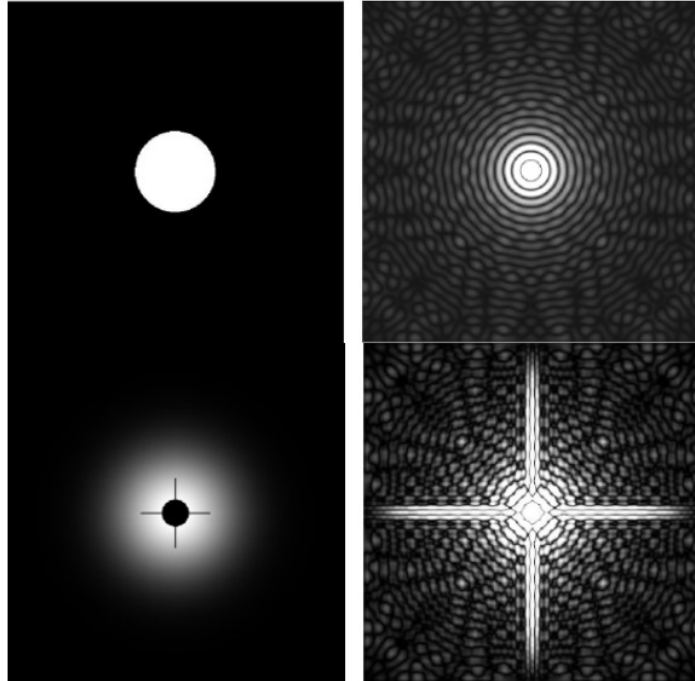


Figure 4: **Top:** Ideal unblocked aperture showing Airy disc pattern **Bottom:** Blocked aperture power distribution with interference effects [1].

Despite the reduced effective area and the lowered resolution due to diffraction caused by aperture blocking, the advantage of using such a construction is that it allows a rigid and compact telescope [1].

3.3 Radiometer

The radiometer is the receiving unit of a radio telescope. It consists of six main parts as seen in Figure(5).

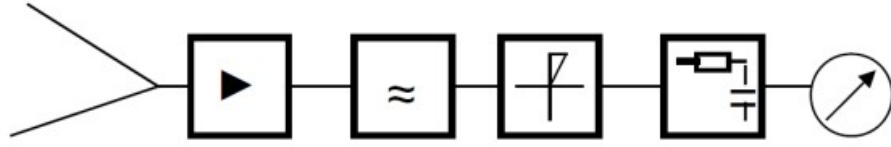


Figure 5: Schematic of a radiometer depicting its various components [1]

The signal enters from the left and the power output is read at the right. The six main parts are:

1. The feed/antenna: The antenna (feed) converts the incoming space waves into electric current with minimal losses. For wavelengths shorter than 0.3 m a simple dipole is used and for smaller wavelengths, a feed is used. Figure(6) shows a typical feed, where the dipole is optimally placed at a distance of $\frac{\lambda}{4}$.

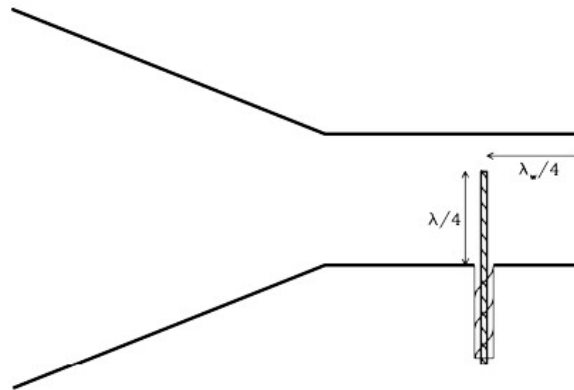


Figure 6: Schematic of the construction of a feed showing the optimised position of the dipole [1]

2. **Amplifier:** The amplifier is located behind the feed. Because radio astronomical sources are faint, the incoming signal needs to be amplified. The simplest amplifier is a transistor. The transistor works such that a strong current between the source and the drain is modulated by the weak signal linked to the gate of the transistor. This leads to an amplification of the faint signal by the order of 10^3 to 10^6 .
3. **Bandpass:** The bandpass is a filter that is used to select a certain frequency range from the entire electromagnetic spectrum.
4. **Diode:** A diode is used as a detector. Since simply integrating the changes in voltage would average out the positive and negative modulations the EM wave recorded at the receiving dipole, to evaluate the energy received we need to square the signal from the amplifier U_{HF} (high-frequency voltage). The detector then measures the voltage U_{det} (detector voltage) where $U_{det} \propto U_{HF}^2$. A diode has strong nonlinear current-voltage characteristics and at its aim-point, we find the square characteristics.
5. **Integrator:** An RC circuit integrator is used to add up all the voltage modulations U_{det} to give the final signal over an integration time Δt .
6. **Backend:** The integrated power of the final signal is read out into a readable data format using the backend.

At Stockert, the receiver is located at the prime focal point which is why it does not have a second dish (the second dish has been removed and is placed near the telescope). The receiving horn of the receiver is a cylindrical waveguide with Chaparral type rings and it is adjusted for a target illumination taper of 12 dB [5, 6].

3.3.1 Radiometer Equation

The radiometer equation in Equation(3) is used to measure the quality of a radio astronomical observation.

$$\Delta T = \frac{T_{sys}}{\sqrt{\Delta\nu \cdot \Delta t}} \quad (3)$$

where ΔT is the uncertainty in the determination of source brightness temperature, T_{sys} is the system temperature as defined in $\Delta\nu$ is the bandwidth and Δt is the integration time. The product of the integration time and the bandwidth is proportional to the amount

of energy received, and the higher the integration time, the more the number of received photons [1].

3.3.2 Spectrometer

A spectrometer is used to determine the Doppler velocity of the 21-cm line emission and their frequency resolution is used because of the narrow HI line. Fast Fourier Transformation spectrometers are used in electronic spectrometers and these limit the spectral channels to powers of 2, typically 2^{14} [1].

3.3.3 Noise

All the elements of the radiometer produce noise, caused by exposure to the environment and the random statistical motion of electrons in each element, which is also proportional to the temperature of the element. The amplifier's noise has the largest effect on the whole system because the noise gets amplified as well and its gain is of the order of 10^3 to 10^6 . Because of this, the amplifier is usually cooled using liquid nitrogen or helium [1]. At Stockert, the first amplifier stage are LNAs (Low Noise Amplifiers) with a noise figure of 0.5dB [5, 6].

4 Calibration using standard Milky Way source

4.1 Theoretical Background

4.1.1 Rayleigh-Jeans Approximation

In radio ranges, we observe wavelengths from dm to sub-mm, which corresponds to frequencies in the range of MHz to THz. The corresponding energy range is $4 \cdot 10^{-9} eV \leq h\nu \leq 4 \cdot 10^{-4} eV$, which is low compared to the average kinetic energy of moving particles in a gas within the Milky Way. So here $h\nu \ll kT$, where h is the Planck constant in units of eV ($h = 4.135 \cdot 10^{-15} eVs^{-1}$), ν is the frequency of the radiation, k is the Boltzmann constant and T is the gas temperature.

We do radio observations around the frequency range of $1.4 GHz$ at Stockert. Our aim is to measure the physical temperature of the source that is being observed. For this, we relate the brightness $B_\nu(T)$ by using the Planck law[1]

$$B_\nu(T) = \frac{2h\nu^3}{c^2} \frac{1}{\exp(\frac{h\nu}{kT}) - 1} \quad (4)$$

Expanding the exponential and using the aforementioned assumption of $h\nu \ll kT$.

$$B_\nu(T) = \frac{2h\nu^2 kT}{c^2} \quad (5)$$

which is the Rayleigh-Jeans approximation for thermal (black body) emission [1]. The consequence of this is that the brightness temperature of an observed source is directly proportional to the brightness and can be further related to intensity and flux. This approximation is sufficient for our use in radio astronomy because of the low frequency regime, where the approximation holds.

4.1.2 Brightness Temperature and Antenna Temperature

A radio telescope does not just receive radiation from the source but also from its whole environment. The main lobe is the antenna's maximum sensitivity that receives about 70% of all the incoming radiation, and the remaining is received by the stray lobes. Due to aperture blocking a significant amount of the incident radiation is collected by the stray lobes.

Apart from the emission from the source of the interest, unwanted superimposed sources of radiation contaminate the incoming radiation and can be classified as:

- the source of interest T_{source}
- the cosmic microwave background T_{CMB}
- the synchrotron radiation of the Milky Way, $T_{syn} \propto \nu^{-2.7}$, and $T_{syn}(\nu = 1420 MHz) \simeq 0.1 K$
- the temperature of the Earth's atmosphere T_{atm}
- the spillover from the receiver T_{spill}
- the thermal noise of the receiving system $T_{receiver}$

All the received radiation adds up linearly to give what is known as the system temperature T_{sys} :

$$T_{sys} = T_{source} + T_{CMB} + T_{syn} + T_{atm} + T_{spill} + T_{receiver} \quad (6)$$

The temperature of the source is faint in comparison to the system temperature and the SNR is minimized by cooling the amplifier, as explained in[1].

While the temperature of the source is the brightness temperature T_B , our observations do not actually find the brightness temperature, but another quantity which is the antenna temperature T_A . This is because of the 21-cm beam, only a narrow part of the telescope's lobe is illuminated by the source, which has a width of a few arcmins. The antenna temperature includes this unrelated background emission.

The relation between the antenna temperature and the brightness temperature is as seen in Equation(7) and needs to be taken into consideration for our calculations.

$$\frac{T_A}{T_B} = \frac{\Omega_{source}}{\Omega_{MainBeam}} \quad (7)$$

where Ω_{source} and $\Omega_{MainBeam}$ are the angular extents of the source and main beam. The antenna temperature is not unique for a given source of interest but depends on the size of the telescope [1].

Thus, for the HI 21-cm line measurements, we need to calibrate the telescope and determine the ratio in Equation(7). For this we use some well-known calibration sources defined in [2] which lists the sources. These sources are sufficiently large and have a well-known flux at the given frequency range and thus their brightness temperature T_B can be measured independently of the telescope size and can be used to calculate the ratio to the antenna

temperature.

Since the antenna temperature depends on the telescope, we aim to convert this into a physical quantity that is independent of the instrument. For this, we define the aperture efficiency as:

$$A_{eff} = \frac{P_{received}}{S_{source}} = \frac{2kT[K]}{S_{source}[Jy]} \quad (8)$$

where $P_{received}$ is the power received from the source and S_{source} is the specific flux.

Using the Rayleigh-Jeans Approximation, and rearranging and substituting values specific to Stockert, we get the conversion from Kelvin to Jansky as:

$$\frac{T[K]}{S_{source}[Jy]} = \frac{A_{eff}}{2k} = \frac{\pi(12.5 \cdot 0.7m)^2}{2 \cdot 1.38 \cdot 10^{-23} \left[\frac{J}{K}\right]} = 0.09 \quad (9)$$

4.2 Calibration Source Observation and Analysis

In this section, we aim to obtain a calibration factor for our observation based on previous literature value of the chosen galaxy source **S7**

4.2.1 Observation

As mentioned in the previous section for meaningful spectral data we need to relate antenna temperature (T_A) with the actual brightness temperature of the system (T_B). For this purpose, we observe and obtain the radio spectrum of **S7**. From [2], we know the actual brightness temperature of **S7** as **96.3 K** for HPBW in the range of Stockert telescope. The brightness temperature observation in the paper has an accuracy of 2%. As seen in [2] the source has a sufficiently bright flux, so spectra were obtained after an integration time (Δt_{int}) of **22s** and with a spectra resolution ($\Delta \nu_{res}$) of **6103.51 Hz**. The integration was well suited for the signal to have statistical uncertainty below 5% for this source. The raw spectral data is given in the Appendix(2.1)

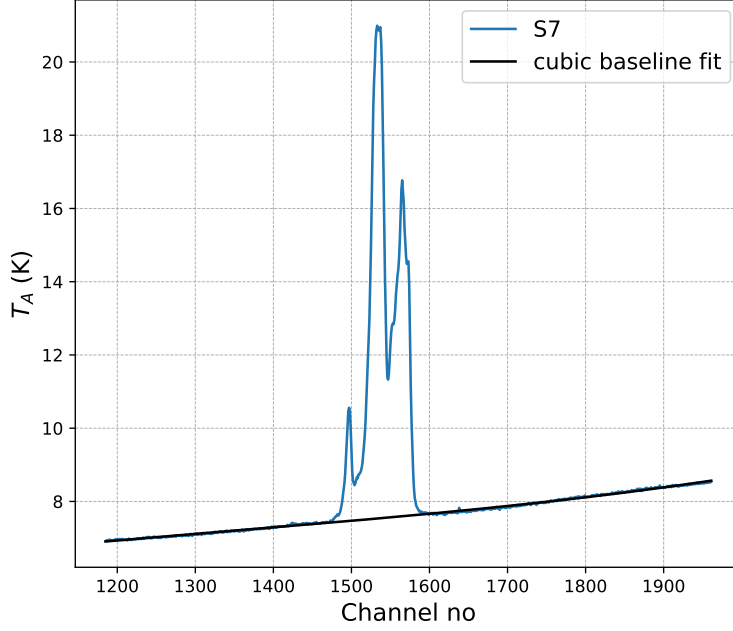


Figure 7: S7 galaxy data. A cubic polynomial was fitted to model the baseline of this spectra

The spectrum was then fitted (masking the peak region) with a cubic polynomial using the python package SCIPY-CURVE FIT, as seen in Figure(7). The background was then subtracted, to obtain a continuum subtracted data. To obtain meaningful data from the spectrum, the x-axis was converted to the radial/recessional velocity of the galaxy using the formulae-

$$v = (1 - \frac{\nu}{\nu_o})c \quad (10)$$

where ν in Hz was derived from the data obtained from telescope post-processing, $\nu_o = \mathbf{1420.41 \text{ MHz}}$ and velocity of light was taken as $\mathbf{299792.458 \text{ kms}^{-1}}$. From Figure(8), we obtain the maximum antennae temperature as $\mathbf{13.45775 \text{ K}}$. The error in obtaining the temperature is the root-mean squared error(RMSE) of the baseline in continuum subtracted data. RMSE error is considered as it has a large weight factor for large errors which are to be particularly considered here. RMSE error is calculated as:

$$\Delta T_A = \sqrt{\sum_{\text{baseline}} T_A^i{}^2 / N(\text{total data points})} \quad (11)$$

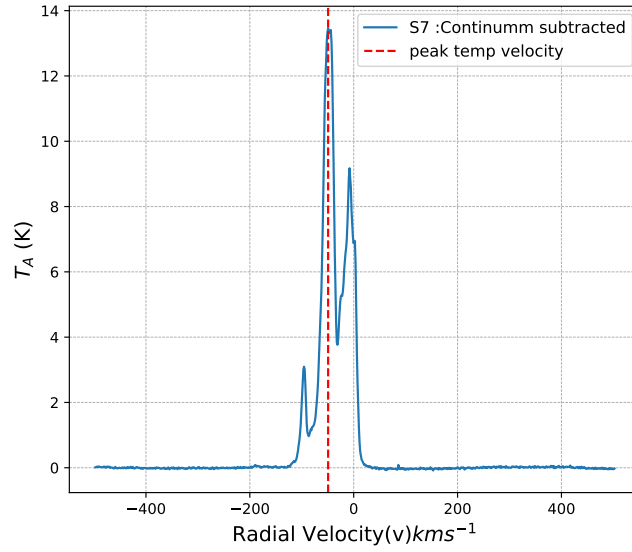


Figure 8: Spectra of S7 plotted w.r.t to radial velocity of galaxy. The other two peaks are signals from the Milky Way galaxy

4.2.2 Determining Calibration factor and system temperature

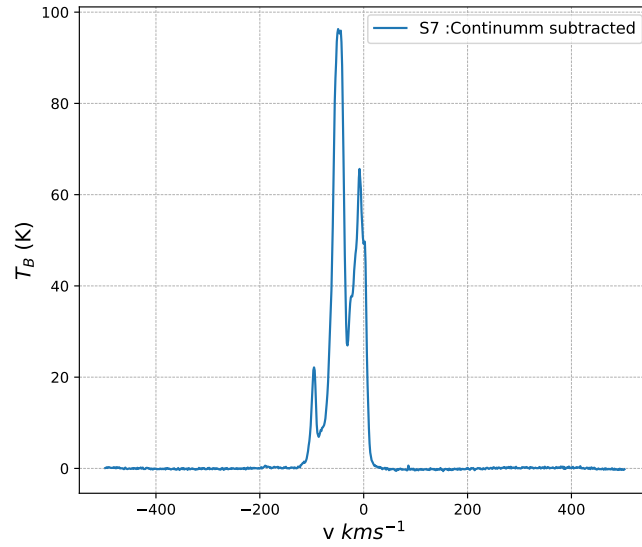


Figure 9: Spectra of S7 plotted as brightness temperature vs radial velocity

For this Figure(8), we derive $\Delta T_A = 0.0531 \text{ K}$. Then the calibration factor alpha was calculated as

$$\alpha = \frac{T_B}{T_A} = \frac{96.3}{13.457 \pm 0.0531} = 7.1557 \pm 0.0282 \quad (12)$$

where the error of α was calculated using the Gaussian error propagation method and implemented by the python package UNCERTAINTIES[7]. Using this calibration factor, the spectrum was plotted once again (as seen in Figure(9)).

The error in peak brightness (ΔT_B), calculated using Eq(11) is **0.216 K**. Then the system temperature calculated from Eq(3) is-

$$T_{sys} = \Delta T_B \sqrt{\Delta t_{int} \Delta \nu_{res}} = 79.214 \text{ K} \quad (13)$$

T_{sys} calculated is on the higher limit of the expected temperature of such a radio telescope system. It can be attributed to the fact there is no cooling of the receiver components, excessive spilling of radio signal and thermal noise from mechanical/electrical components in the telescope system.

5 Observing a nearby Galaxy

In this section, we aim to observe the HI line of the galaxy at the radio frequency of 1420 MHz. From the spectra, various characteristics parameters of the galaxy are derived and compared with previous observations of the same.

5.1 Observing Galaxy candidate

From typical values Table(3), we see that the possible candidates have comparatively a low magnitude, so a larger integration time is needed. From Eq(3) and defining $\text{SNR} = (T_B)/(\Delta T_B)$, the integration time could be calculated by

$$\Delta t_{int} = (\text{SNR}^2) \frac{T_{sys}^2}{T_B^2 \Delta \nu} \quad (14)$$

Putting in typical value and for an SNR percentage of 10% we need an integration time of ≈ 15 mins.

At first **NGC 4736** was observed using the telescope with an integration time of about 15 mins. But in the data pre-processing it was seen that SNR is too low for resolving the HI line properly. This could be attributed to the large value of the width of the HI line and also the faint flux compared to other candidates. The spectrum for this observation is shown in Appendix(8.2).

NGC 4395/UGC 007524 was observed using the Stockert Telescope with an integration time(Δt_{int}) of **902 s** or about 15 mins. The parameters of the galaxy are

Galaxy	RA	Dec	Radial Vel (km/s)	Extend (arcmin)	HI 21 Mag	HI 21 50pc width (km/s)
NGC4395	186.4575	33.5461	313	13.18	11.53	98

Table 3: The galaxy data was taken from [HEASARC](#) browser for the NEARGALCAT - Updated Nearby Galaxy Catalog [3].

Further, it is a spiral galaxy of type AB i.e. **SAB** [8]. It is found to host an AGN nucleus of Seyfert Type I [9]. From the paper [10] the integrated or total mass of the galaxy was calculated with a mass-luminosity ratio of 20.8. It was also stated that the galaxy is de Vaucouleurs type 3 galaxy.

Survey/ Paper	Telescope	Resolution $km s^{-1}$	Heliocentric radial vel $km s^{-1}$	Integrated Flux $Jy km s^{-1}$	M_{HI} ($10^{10} M_{\odot}$)	M_{total} ($10^{10} M_{\odot}$)
Integrated Masses of Galaxies [10]	91m radio telescope at NRAO	6.6	315	176.8	–	11.4
Neutral Hydrogen Observations Of a Large Sample of Galaxies [11]	91 m telescope at NRAO	22	318	–	–	10.09
Arecibo Legacy Fast ALFA Survey [12]	Arecibo 305 m telescope	11	316	301.08	0.112	–
A neutral hydrogen mapping survey of large galaxies. I. Observations. [13]	91 m telescope at NRAO	22	320	301.1	–	–

Table 4: Literature Parameters of NGC 4395 derived from various radio telescope observations

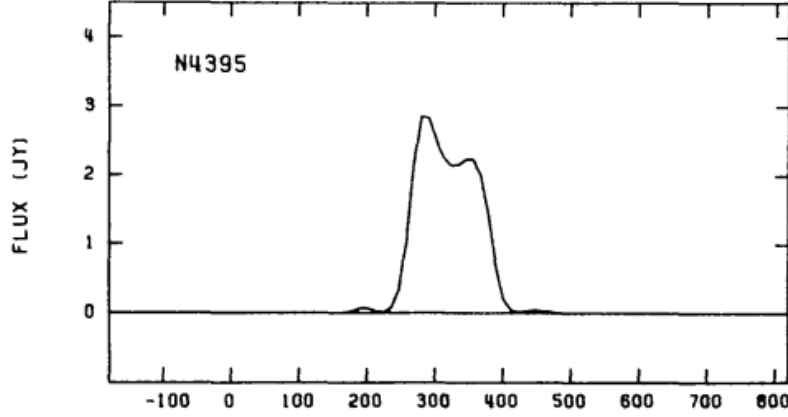
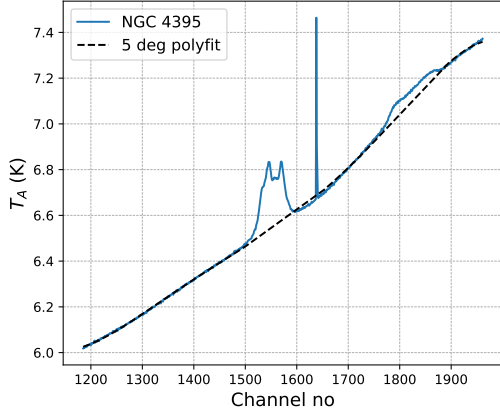


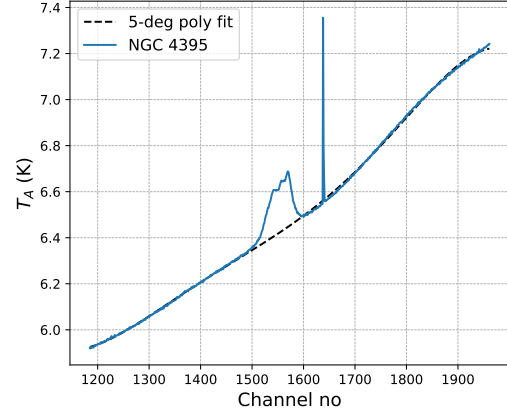
Figure 10: HI spectrum of NGC 4395 as observed from 91m radio telescope at the National Radio Astronomy Observatory [13] with a resolution of $22 km s^{-1}$

5.2 Calibrating galaxy spectrum

After obtaining the spectrum (seen in Figure(11a)), a method to actively isolate the HI lines is an 'offset measurement'. In this offset measurement, the radio telescope is pointed slightly away from the galaxy target centre and beyond the influence of the telescope beam extent i.e. an offset of at least 0.5° . We see that we obtain a spectrum with features similar to peaks as in the previous figure but the HI of the target galaxy features have completely disappeared. In both the spectrum, the peak area was masked and the baseline was fitted with a **polynomial of degree 5** using similar methods mentioned in the previous section (Figure(11)).



(a) Raw spectrum



(b) offset spectrum

Figure 11: HI and offset spectrum of NGC 4395

After subtracting the continuum from both the HI line spectra and offset measurement, the HI region still needs to be enhanced. For this, the continuum subtracted offset spectrum was subtracted from the subtracted main spectrum containing the HI lines. So we obtain an enhanced HI line with the double horn feature (as seen in Figure(12)). The change in the x-axis to units of radial velocity, as done in the previous section using Eq(10), was implemented here too.

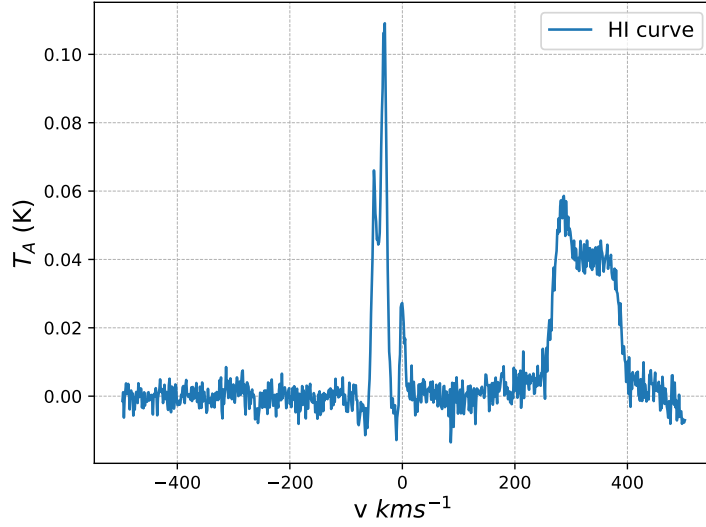


Figure 12: Radio spectrum of NGC 4395 with 'double-horn' shaped HI lines

Then the temperature axis was calibrated with α from Eq(12). So now we can obtain a zoomed-in view of the HI lines of the galaxy and the y-axis indicates the brightness temperature(Figure(13)).

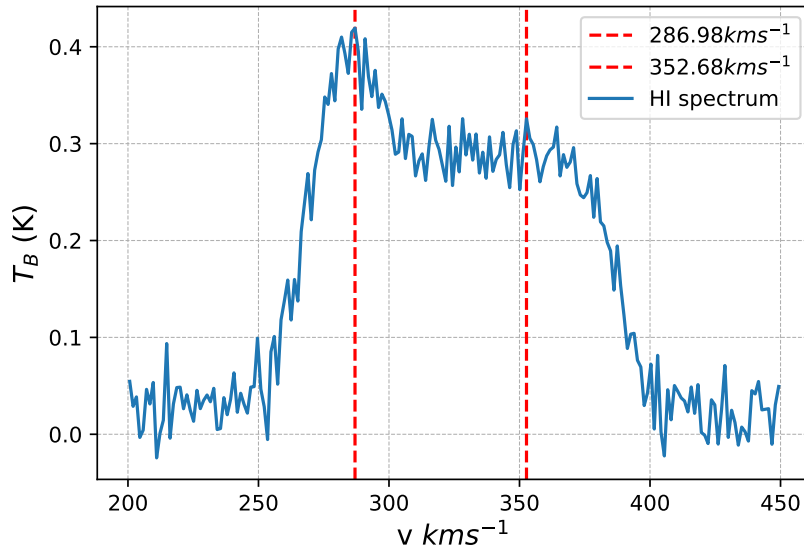


Figure 13: HI line spectrum of NGC 4395 plotted as its brightness temperature vs radial velocity

The recessional/radial velocity(v_{rec}) of HI line is obtained from the average of the velocity of the two double-horned peaks. From Figure(13), it was obtained to be **319.829 kms⁻¹**. From this value, the distance to the galaxy can be determined using Hubble-Lemaitre law $v_{rec} = H_0 d$, where H_0 is the Hubble's constant and d is the radial distance to the galaxy.

$$d = \frac{v_r}{H_0} = \frac{319.829(kms^{-1})}{75(kms^{-1}Mpc^{-1})} = \mathbf{4.264\ Mpc} \quad (15)$$

The RMSE mean of the baseline of the HI spectrum was calculated to be **0.0332 K**. The peak brightness temperature ($T_{B\ max}$) was found to be **0.42 ± 0.0332K**. But if we calculate the Gaussian error arising from α we see a larger error in $T_{B\ max}$ of about **0.21 K**. From this maximum brightness temperature value, we calculated the specific flux using Eq(9), to be **4.659 ± 1.89Jy**. Here we have considered the Gaussian error instead of the RMSE error as it suggests larger deviations. We can see this value of specific flux is comparable with the literature spectrum in Figure(10).

The integrated flux was obtained considering the HI region within 250kms⁻¹ to 400kms⁻¹. Thus integration was implemented in Python using the NUMPY *trapz* function. The total integrated flux ($\int S_\nu d\nu$) was found to be **318.587 ± 1.257 Jy kms⁻¹**. Here also we have considered the Gaussian error arising from the value of α . This value is quite comparable with the literature values in Table(4).

The large error of α and $T_{B\ max}$ may be attributed to non-optimised spectrum subtraction done. As seen in Figure(12), the baseline around the HI double-horn structure is not centred around 0 of the y-axis. This may be a contributing factor to the large deviations. This could have been eliminated by a better resolution or larger integration time.

5.3 Calculating different masses of galaxy

HI mass of a galaxy can be calculated as an approximated column density for hydrogen gas. Taking the approximation of an optically thin gas and accounting for the intensity fall-off with the square of the radial distance, the formulae for HI mass can be given by[1]-

$$\frac{M_{HI}}{M_\odot} \approx 2.36.10^5 \left(\frac{r}{[Mpc]} \right)^2 \int \frac{S_\nu}{[Jy]} \frac{dv}{[kms^{-1}]} \quad (16)$$

Inserting the values obtained, we get

$$\frac{M_{HI}}{M_\odot} = (\mathbf{1.3699 \pm 0.005}).10^9$$

As M_{HI} is at most only 10% of the total baryonic mass, total baryonic mass of the galaxy can be estimated to be

$$\frac{M_{baryonic}}{M_{\odot}} = (1.3699 \pm 0.005).10^{10}$$

But we know that even after approximating the baryonic mass as the total luminous mass of the galaxy, there is still some remaining mass of the galaxy unaccounted for. So the total mass of the galaxy can be estimated using the mass-to-luminosity ratio derived for local objects. As mentioned before, we know that that NGC 4395 is a spiral galaxy of type AB and in de Vaucouleurs scale a type 3 galaxy. In [14] the mass to luminosity ratio is about 6 for SAB type galaxy (here they have considered the luminosity of $B-$ band). Also from Figure(2.9) in the manual([1]), for such spiral galaxy, the ratio is above 6. Though in [10] the ratio (based on Holumberg photographic magnitude) is as high as 20. From all these considerations we have considered a **mass to luminosity ratio** of **7**. So the total mass of the galaxy is then given by:

$$\frac{M_{total}}{M_{\odot}} = (9.589 \pm 0.0378).10^{10}$$

The estimated total mass is lower than the other literature value. It may be attributed to reasons like not considering a suitable mass-to-luminosity ratio for the calculation. Also, the non-negligible error on the integrated flux may be a contributing factor.

6 Determining the distance of a pulsar

6.1 Chosen Pulsar and Integration Time

The first step is to choose a specific pulsar from the list made in Section(2.2). The pulsar chosen is **B0329+54**. The estimated integration time to detect the pulsar signal was about 30 minutes. With the Stockert telescope, we observe the pulsar signals at 1.4 GHz.

6.2 Data Reduction Process

The observation of the pulsar involved a combined analysis and saving of each measured profile as opposed to integrating a given signal over time. Every $218 \mu s$, a new spectrum is recorded and stored. An important step to do this was to change the mode of the radio telescope from the HI mode to the pulsar backend mode.

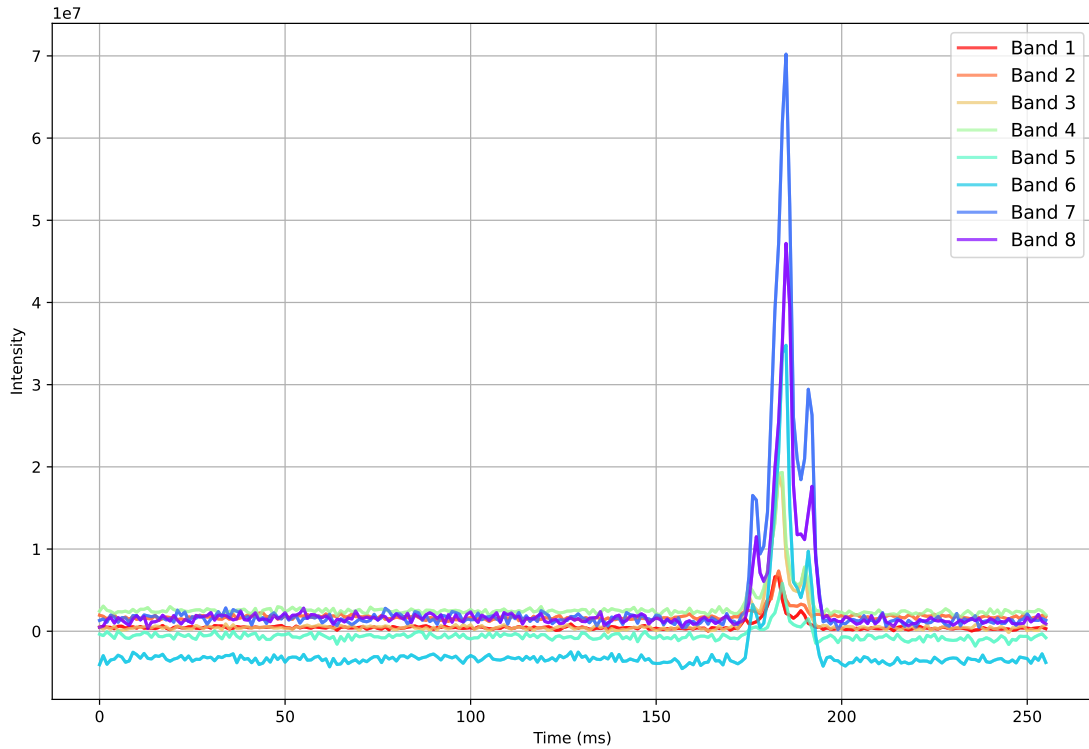


Figure 14: The intensity profiles in arbitrary units of the 8 bands of the folded pulse of the pulsar.

Now, the signal obtained from the pulsar is divided into eight sub-bands as seen in Figure(14). The next step involves folding all the measured profiles to obtain a folded intensity spectrum over one period of the pulsar. Folding involves overlapping and adding the pulses from the eight bands. This yields the period of the pulsar as well, which is found to be $714.46ms$. The folded spectrum of one period is then divided into 256 channels, and for each channel, the time period corresponds to $t_c = 714.46ms/256 = 2.790859375ms$. Using the eight bands' folded profiles, the 256 channels, and the knowledge about the bandpass, we calculate the central frequency of the frequency bands. The whole bandpass transmits 98.4 MHz, the upper limit is 1430.391 MHz and divided into eight bands each with a width of 12.3 MHz.

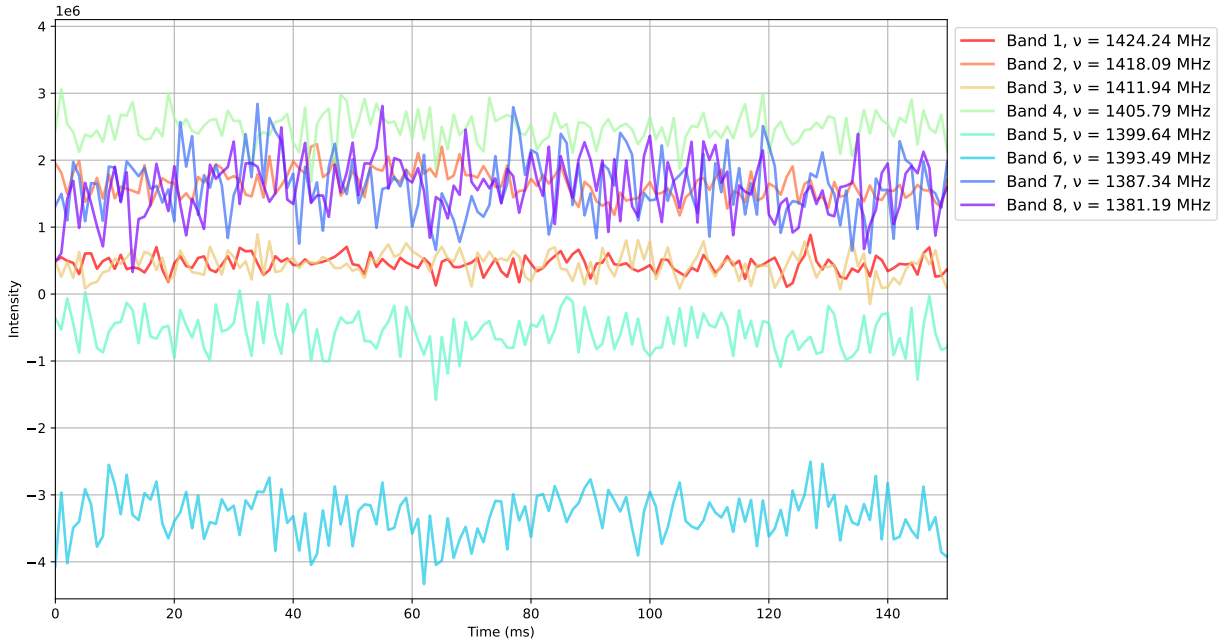


Figure 15: A section of the intensity profiles of the 8 bands to depict the separation, along with their central frequencies.

Since the bands have different positions of the pulses, we apply a Gaussian fit to each of the eight bands to determine this position. The fits for all eight bands can be found in the appendix section 8.3. The Gaussian fit for one band is seen in Figure(16) and the values of the obtained positions from the fit are in Table(5)

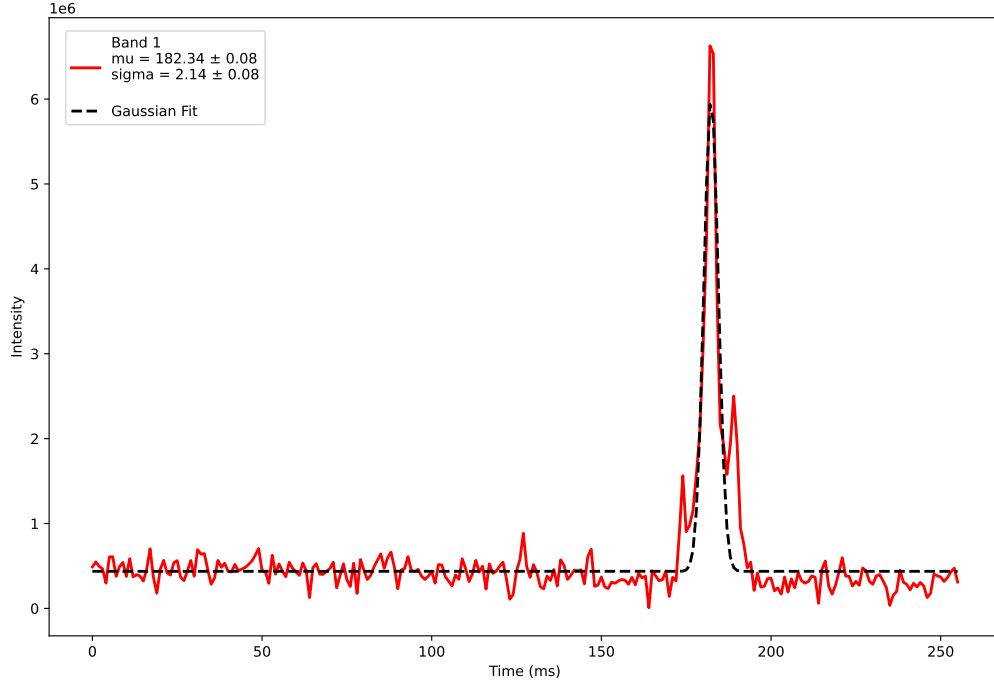


Figure 16: Gaussian Fit performed on the intensity profile of the first band.

Next, the time of arrival is calculated, by multiplying the position of the centre of the pulse obtained from the fits with the time period of the channel calculated in

$$t = \mu \cdot t_c \quad (17)$$

The final results obtained from the fit for the position and the arrival times with the errors are displayed in Table(5).

Band Number	Central Frequency (MHz)	Pulse Position	Arrival time (ms)
1	1424.24	182.34 ± 0.08	508.88 ± 0.21
2	1411.94	182.97 ± 0.12	510.64 ± 0.34
3	1399.64	183.12 ± 0.09	511.07 ± 0.24
4	1387.34	183.26 ± 0.07	511.46 ± 0.19
5	1375.04	183.75 ± 0.13	512.82 ± 0.36
6	1362.74	184.18 ± 0.07	514.02 ± 0.20
7	1350.44	184.65 ± 0.11	515.34 ± 0.30
8	1338.14	184.84 ± 0.08	515.86 ± 0.23

Table 5: Table depicting the position of the pulse and the calculated arrival time for the eight bands obtained from the parameters from the Gaussian fits.

The next step towards the calculation of the dispersion measure is to evaluate the temporal separation between the arrival times of the low and high frequency pulsar signal. The time of the first and last signals is calculated and used as the separation.

$$\tau = t_8 - t_1 = 6.985 \pm 0.31 \text{ ms} \quad (18)$$

Now we calculate the dispersion measure. The formula used for this is derived from the details given in the lab manual [1]. The temporal delay is:

$$\tau(\nu) = 4.149 \frac{[GHz]^2}{\nu^2} \int_0^D \frac{n_e}{[cm]^{-3}} dl [s] \quad (19)$$

And the dispersion measure is:

$$DM = \int_0^D n_e dl [pc \text{ cm}^{-3}] \quad (20)$$

The final formula that we use is:

$$\left(\frac{DM}{[cm^{-3} PC]} \right) = \left(\frac{\tau}{[ms]} \right) \frac{1}{4.149} \left[\left(\frac{\nu_1}{[GHz]} \right)^{-2} - \left(\frac{\nu_2}{[GHz]} \right)^{-2} \right]^{-1} ms^{-1} \quad (21)$$

Substituting the values for the above equation, we obtain the dispersion measure as:

$$DM = 26.404 \pm 6.09 \text{ pc cm}^{-3} \quad (22)$$

The obtained dispersion measure is close to the expected value of 26.7641 cm^{-3} . From the dispersion measure, the distance to the pulsar can be calculated from the electron volume density (n_e).

$$l = \frac{DM}{n_e} \quad (23)$$

To obtain a value for the electron density, the Yao, Manchester and Wang model [15] was used (YMW16 model). A website [16] from the Australia Telescope National Facility based on the YMW16 model was used to calculate the electron density that would hold for our pulsar. After entering the galactic coordinates for the pulsar, the electron density was calculated as $n_e = 0.2217 \text{ cm}^{-3}$. Using this, the distance is then calculated to be:

$$l = 1.191 \pm 2.75 \text{ kpc} \quad (24)$$

7 Conclusion

In this lab, we performed analysis on the observations made through the 25-m Stockert Radio telescope at 1420 MHz. We explored the characteristics features of this telescope and discussed its limitations. We observed NGC 4395 and performed a spectral analysis on its HI spectrum. This galaxy spectrum was calibrated using the data galaxy 'S7'. A calibration factor of $\alpha = \mathbf{7.155 \pm 0.0282}$ was derived and the system temperature was estimated to be $\mathbf{79.214\ K}$. From the HI spectrum of the recessional velocity of the galaxy was derived to be $\mathbf{319.829\ kms^{-1}}$. The Specific flux at the peak brightness temperature was found to be $\mathbf{4.659 \pm 1.89\ Jy}$. Upon integrating in the HI region of the spectrum, the total integrated spectrum of the galaxy was found to be $\mathbf{318.587 \pm 1.257\ Jy\ kms^{-1}}$. From this the M_{HI} was found to be $(\mathbf{1.3699 \pm 0.005}) \cdot 10^9\ M_{\odot}$. Accounting for both the luminous and non-luminous masses of the galaxy, the total mass of the galaxy was derived to be $(\mathbf{9.589 \pm 0.0378}) \cdot 10^{10}\ M_{\odot}$.

The deviations of the values from observations in literature can be explained by large deviations in calibration factor and offsets in the flux in the HI region of the galaxy. This can be improved by longer integration time or achieving a better SNR. So cooling of the receiver units may lead to substantial improvement of the measurements. Further, a better HI spectrum could have been obtained by more accurate offset measurements of the galaxy spectrum, using a narrower beam width. A narrower beam would also lead to better resolution of the spectrum and more accurate results of the integrated flux.

The final part was to observe a pulsar and to calculate the dispersion measure and its distance. The dispersion measure was found to be $\mathbf{26.404 \pm 6.09\ pc\ cm^{-3}}$ and the distance $\mathbf{1.191 \pm 2.75\ kpc}$, which are close to the values expected when compared with the ATNF catalogue. The errors in the pulsar observation could be reduced by improving the SNR for the bands with a longer integration time and changing the bandpass filter values. The value of the electron density is also unpredictable, given the nature of the ISM and the model used.

8 Appendix

8.1 Source Galaxy Data

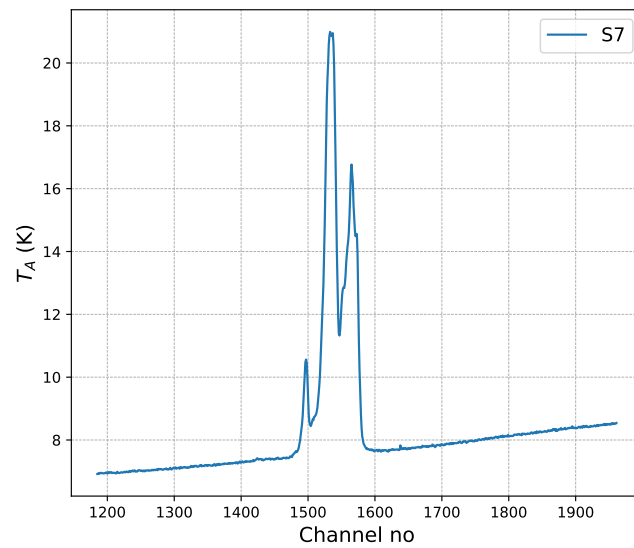


Figure 17: Raw spectrum of S7 plotted as vs channel no vs antenna temperature

8.2 Galaxy observed

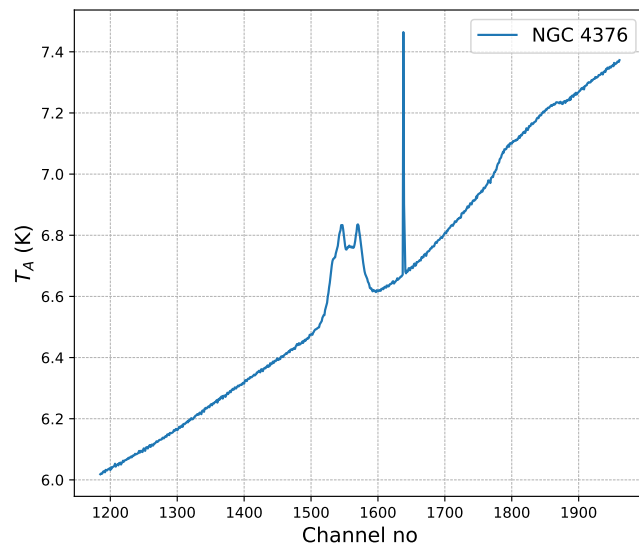


Figure 18: Raw spectrum of NGC 4376 plotted as channel no vs antenna temperature

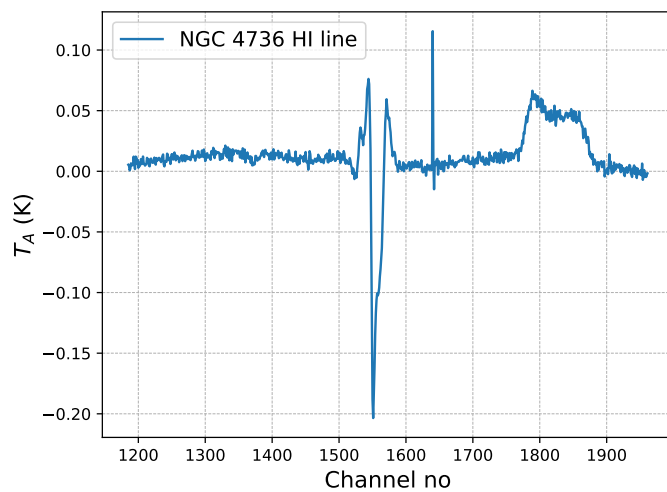


Figure 19: Spectrum of NGC 4736 after continuum subtraction and subtraction of offset spectrum.

8.3 Gaussian Fits for Pulsar

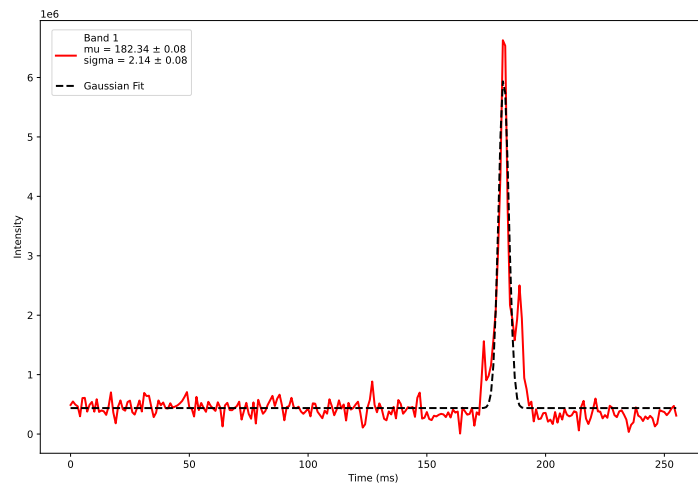


Figure 20: Gaussian fit for Band 1

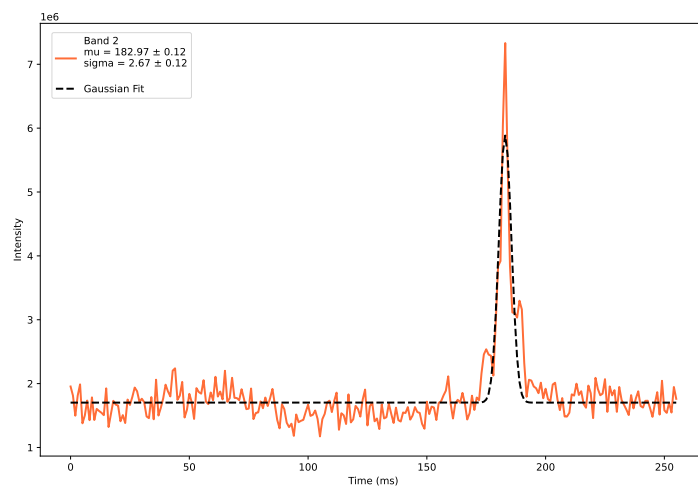


Figure 21: Gaussian fit for Band 2

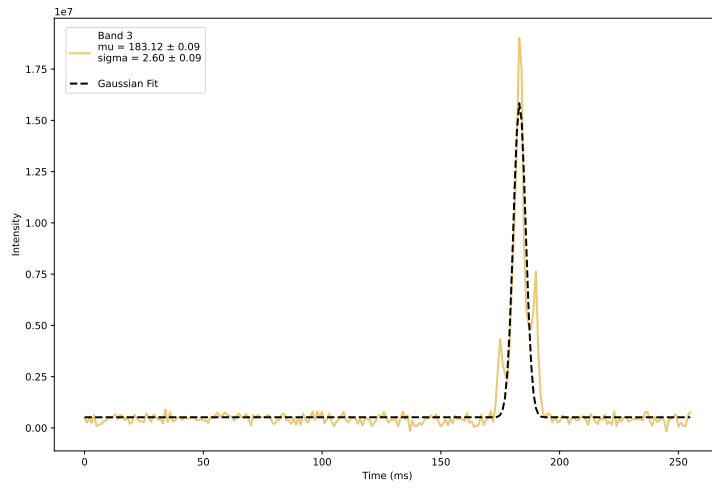


Figure 22: Gaussian fit for Band 3

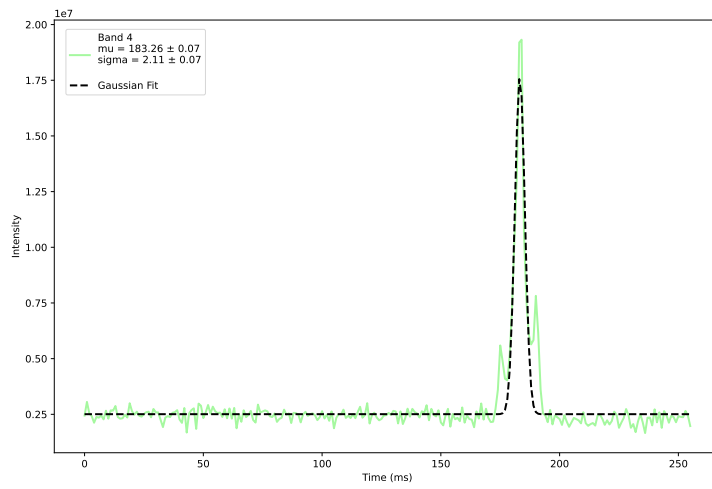


Figure 23: Gaussian fit for Band 4

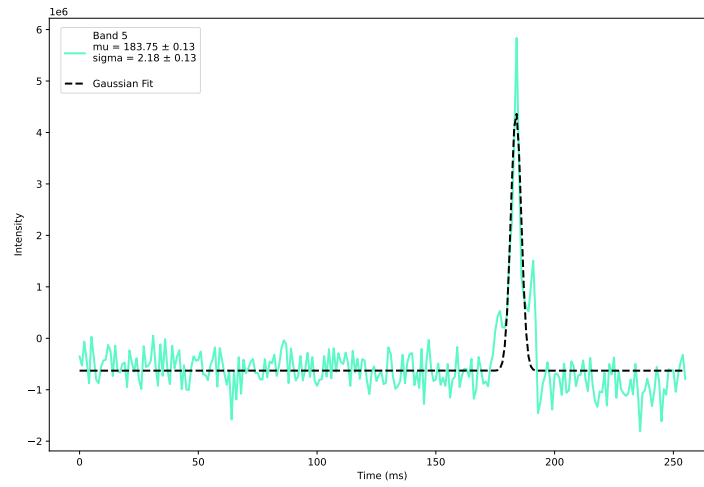


Figure 24: Gaussian fit for Band 5

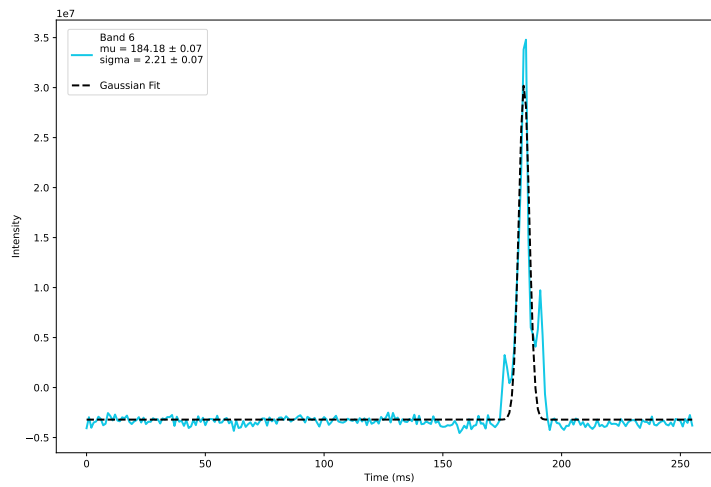


Figure 25: Gaussian fit for Band 6

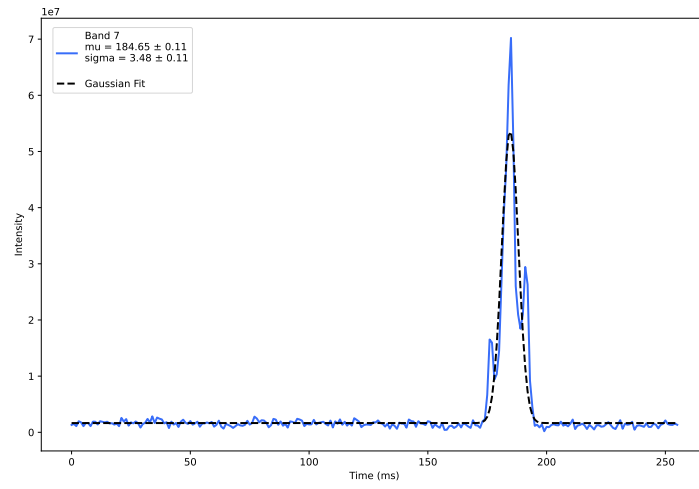


Figure 26: Gaussian fit for Band 7

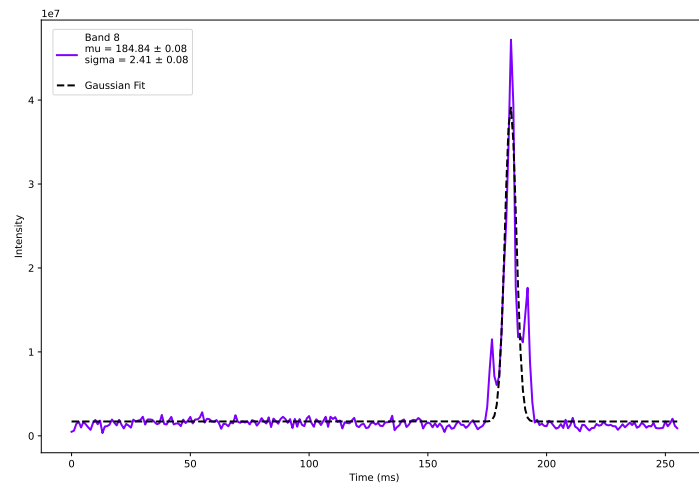


Figure 27: Gaussian fit for Band 8

References

- [1] Jürgen Kerp. *Radio astronomical practical course at the Stockert 25-m telescope*. English. Version 1.0. University of Bonn, Physics Department.
- [2] P. M. W. Kalberla, U. Mebold, and K. Reif. “Brightness temperature calibration for 21-cm line observations”. In: 106.2 (Feb. 1982), pp. 190–196.
- [3] Igor D. Karachentsev, Dmitry I. Makarov, and Elena I. Kaisina. “Updated Nearby Galaxy Catalog”. In: 145.4, 101 (Apr. 2013), p. 101. DOI: [10.1088/0004-6256/145/4/101](https://doi.org/10.1088/0004-6256/145/4/101). arXiv: [1303.5328](https://arxiv.org/abs/1303.5328) [astro-ph.CO].
- [4] R. N. Manchester et al. “The Australia Telescope National Facility Pulsar Catalogue”. In: 129.4 (Apr. 2005), pp. 1993–2006. DOI: [10.1086/428488](https://doi.org/10.1086/428488). arXiv: [astro-ph/0412641](https://arxiv.org/abs/astro-ph/0412641) [astro-ph].
- [5] Astroteiler Stockert e.V. *Technik, Zahlen und Videos*. Accessed on September 14, 2023. URL: <https://www.astroteiler.de/technik-zahlen-und-videos/>.
- [6] Astroteiler Stockert e.V. *Links zu externen Seiten*. Accessed on September 14, 2023. URL: <https://www.astroteiler.de/links-zu-externen-seiten/>.
- [7] Ericnbs; O. LEBIGOT. *Welcome to the uncertainties package*. URL: <https://pythonhosted.org/uncertainties/>.
- [8] Ronald J. Buta. “The systematics of galaxy morphology in the comprehensive de Vaucouleurs revised Hubble-Sandage classification system: application to the FIGFI sample”. In: 488.1 (Sept. 2019), pp. 590–608. DOI: [10.1093/mnras/stz1693](https://doi.org/10.1093/mnras/stz1693). arXiv: [1906.08124](https://arxiv.org/abs/1906.08124) [astro-ph.GA].
- [9] Ji-Feng Liu and Joel N. Bregman. “Ultraluminous X-Ray Sources in Nearby Galaxies from ROSAT High Resolution Imager Observations I. Data Analysis”. In: 157.1 (Mar. 2005), pp. 59–125. DOI: [10.1086/427170](https://doi.org/10.1086/427170). arXiv: [astro-ph/0501309](https://arxiv.org/abs/astro-ph/0501309) [astro-ph].
- [10] J. R. Dickel and H. J. Rood. “Integrated masses of galaxies.” In: 223 (July 1978), pp. 391–409. DOI: [10.1086/156274](https://doi.org/10.1086/156274).
- [11] J. R. Fisher and R. B. Tully. “Neutral hydrogen observations of a large sample of galaxies.” In: 47 (Dec. 1981), pp. 139–200. DOI: [10.1086/190755](https://doi.org/10.1086/190755).

- [12] Martha P. Haynes et al. “The Arecibo Legacy Fast ALFA Survey: The ALFALFA Extragalactic H I Source Catalog”. In: 861.1, 49 (July 2018), p. 49. DOI: [10.3847/1538-4357/aac956](https://doi.org/10.3847/1538-4357/aac956). arXiv: [1805.11499](https://arxiv.org/abs/1805.11499) [astro-ph.GA].
- [13] A. H. Rots. “A neutral hydrogen mapping survey of large galaxies. I. Observations.” In: 41 (Aug. 1980), pp. 189–209.
- [14] S. M. Faber and J. S. Gallagher. “Masses and mass-to-light ratios of galaxies.” In: 17 (Jan. 1979), pp. 135–187. DOI: [10.1146/annurev.aa.17.090179.001031](https://doi.org/10.1146/annurev.aa.17.090179.001031).
- [15] J. M. Yao, R. N. Manchester, and N. Wang. “A NEW ELECTRON-DENSITY MODEL FOR ESTIMATION OF PULSAR AND FRB DISTANCES”. In: *The Astrophysical Journal* 835.1 (Jan. 2017), p. 29. DOI: [10.3847/1538-4357/835/1/29](https://doi.org/10.3847/1538-4357/835/1/29). URL: <https://doi.org/10.3847%2F1538-4357%2F835%2F1%2F29>.
- [16] Australia Telescope National Facility. *The YMW16 Electron-Density Model*. Accessed on September 14, 2023. 2017. URL: <https://www.atnf.csiro.au/research/pulsar/ymw16/>.